

1 **Causal and uncertainty-aware digital-twin framework for ultra-low-noise geoscientific inertial sensors**

ha formattato: Colore carattere: Testo 1

2  
3  
4 Antonino D'Alessandro

5 Istituto Nazionale di Geofisica e Vulcanologia, Osservatorio Nazionale, Rome, Italy

6 [antonino.dalessandro@ingv.it](mailto:antonino.dalessandro@ingv.it)

ha formattato: Colore carattere: Testo 1

ha formattato: Colore carattere: Testo 1

7  
8  
9 **Abstract**

10 Ultra-low-noise inertial sensors are a cornerstone of modern geoscientific instrumentation, enabling high-  
11 resolution observations across seismology, geodesy, gravimetry, and vibration isolation. Achieving and reliably  
12 predicting their performance requires a rigorous treatment of physical causality, noise propagation, and  
13 uncertainty, particularly in force-feedback architectures operating near fundamental limits. In this study, we  
14 introduce a causal and uncertainty-aware digital-twin framework for the design and metrological assessment  
15 of ultra-low-noise geoscientific inertial sensors. The proposed framework integrates mechanical dynamics,  
16 force-feedback control, transduction, and digital acquisition within a physically realisable model that explicitly  
17 enforces causality and stability constraints. Starting from a minimal equation-of-motion description, the digital  
18 twin is formulated in the frequency domain to construct causal transfer functions and a comprehensive noise-  
19 budget model. The framework enables the systematic separation of fundamental thermal noise limits from  
20 implementation-dependent noise sources, including readout, actuation, and digital acquisition effects. We  
21 introduce quantitative performance metrics based on self-noise spectra, dominant noise regimes, crossover  
22 frequencies, and near-plateau bandwidths, allowing complex spectral behaviour to be condensed into  
23 actionable design indicators. Parameter uncertainties are propagated through the digital twin to provide  
24 uncertainty-aware performance estimates and robustness diagnostics. Through a series of illustrative analyses,  
25 we demonstrate how the proposed digital twin supports informed design trade-offs, identifies performance  
26 bottlenecks, and prevents non-physical or overly optimistic sensitivity estimates arising from non-causal  
27 modelling assumptions. While focused on inertial sensors, the methodology is general and transferable to other

28 classes of geoscientific instruments. The framework provides a transparent and extensible foundation for next-  
29 generation sensor design, virtual experimentation, and metrologically consistent performance prediction.

## 32 1. Introduction

33 The design and metrological assessment of ultra-low-noise inertial sensors for geoscientific applications  
34 remains a central challenge in measurement science and engineering. These sensors — including broadband  
35 seismometers, compact accelerometers, [MEMS-based seismic sensors \(D'Alessandro and D'Anna, 2013\)](#), and  
36 advanced gravimetric devices (Prasad et al., 2022) — are critical for resolving weak ground motions across  
37 broad frequency bands, enabling high-precision environmental monitoring, earthquake early warning, and  
38 advanced observational geodesy. In practice, instrument performance is constrained by a combination of  
39 fundamental thermomechanical limits and implementation-dependent noise sources such as thermal  
40 (Brownian) noise of mechanical suspensions, readout electronics noise, quantization error in digital  
41 acquisition, and control-loop artefacts (Ubhi et al., 2022; Zhao et al., 2022; van Dongen et al., 2023).

42 Traditional sensor development has often proceeded through incremental improvements of individual  
43 components, with performance characterised post-facto via laboratory calibration and field testing. While such  
44 approaches are effective for benchmarking specific prototypes, they provide limited insight into the system-  
45 level trade-offs between sensitivity, bandwidth, dynamic range, and robustness, particularly when uncertainty  
46 propagation across the entire measurement chain is of interest. The need for rigorous uncertainty frameworks  
47 in sensor design is well recognised in inertial navigation and metrology communities, where stochastic error  
48 modelling and error budgeting have been emphasised (El-Sheimy et al., 2020).

49 In parallel, the concept of a digital twin has emerged as a powerful paradigm for unifying physics-based  
50 simulation with real-time measurement data, enabling advanced prediction, optimisation, and uncertainty  
51 quantification in complex engineered systems. Digital twin methodologies have been extensively reviewed in  
52 industrial and infrastructure domains, highlighting their potential for model-based monitoring and decision  
53 support (Sun et al., 2024; Carlin et al., 2024). Recent developments have increasingly focused on uncertainty-  
54 aware and physics-informed digital twins for metrological applications, with particular emphasis on  
55 traceability, virtual experimentation, and hybrid modelling approaches that combine physical models with

ha formattato: Colore carattere: Testo 1

56 data-driven components (e.g., Wright and Davidson, 2024; Maculotti et al., 2024; Sun et al., 2024). In  
57 metrology, digital twins are gaining traction as tools for virtual calibration, uncertainty evaluation, and  
58 traceability analysis across diverse measurement systems, including coordinate measuring machines, optical  
59 scanners, and virtual metrological experiments (Vlaeyen et al., 2021; Poroskun et al., 2022).

60 Despite these advances, the digital-twin literature remains fragmented with respect to sensor-centric, causal,  
61 and uncertainty-aware frameworks that encompass both physical dynamics and digital acquisition processes.  
62 Many digital twin formulations in metrology still focus on high-level concepts or specific subsystems, without  
63 enforcing physical causality and realisability constraints essential for accurate modeling of closed-loop, force-  
64 feedback inertial sensors. Furthermore, the representation and propagation of uncertainty through the digital  
65 twin's internal variables and across the physical-digital boundary is often treated qualitatively or post hoc  
66 rather than systematically (Ríos et al., 2020).

67 In the field of inertial sensing, contemporary research continues to push performance boundaries through  
68 innovative mechanics and novel readout schemes, such as interferometric sensing with enhanced dynamic  
69 range and low noise floors (Kranzhoff et al., 2023), as well as advanced tilt and vibration measurement systems  
70 that delineate thermal and readout noise dominance across frequency (Bai et al., 2025). In particular, recent  
71 work has demonstrated significant progress in ultra-low-noise interferometric readout systems and compact  
72 inertial sensor architectures, pushing noise floors closer to fundamental limits while maintaining practical  
73 deployability (Carter et al., 2024; Carter et al., 2025; Bai et al., 2025). ~~These efforts~~ These efforts, together with  
74 recent reviews on MEMS-based seismic instrumentation and low-noise inertial sensing technologies  
75 (D'Alessandro et al., 2019), underscore the importance of integrated noise budgeting and uncertainty analysis,  
76 yet a comprehensive, unified framework that couples physical system dynamics, sensor signal chains, and  
77 digital data acquisition with rigorous uncertainty propagation is still absent.

78 This manuscript addresses these gaps by introducing a causal and uncertainty-aware digital-twin framework  
79 for ultra-low-noise geoscientific inertial sensors. The framework enforces physical causality and realisability  
80 constraints while systematically propagating uncertainty from mechanical parameters and control elements  
81 through to spectral performance metrics. It integrates mechanical modelling, transduction chains, force-  
82 feedback architectures, and digital acquisition within a single, physically consistent representation (Fig. 1). By  
83 decomposing self-noise into fundamental and implementation-dependent contributions and identifying

ha formattato: Colore carattere: Testo 1

84 dominant noise regimes, the framework facilitates quantitative evaluation of design choices and metrological  
85 limits.

86 Rather than relying on experimental datasets, the methodology is conceived as a design-stage tool to guide  
87 sensor architecture choices and parameter selection prior to hardware realisation. The remainder of this paper  
88 is organised as follows: Section 2 formalises design requirements and problem scope; Section 3 presents the  
89 digital-twin architecture; Section 4 develops the comprehensive noise model; Sections 5 and 6 analyse spectral  
90 performance and design trade-offs; Section 7 synthesises performance metrics and optimisation strategies;  
91 Section 8 discusses broader implications and limitations; and Section 9 concludes with final remarks.

92

93

## 94 **2. Design requirements and problem formulation**

95 The design of ultra-low-noise inertial sensors for geoscientific applications constitutes a multi-objective  
96 optimisation problem in which sensitivity, bandwidth, dynamic range, robustness, and practical  
97 implementation constraints must be addressed simultaneously. Unlike post-deployment performance  
98 assessment or component-level optimisation approaches, the present study formulates the sensor design  
99 problem explicitly at the pre-implementation stage, adopting a system-level perspective aimed at predicting  
100 achievable performance prior to hardware realisation.

101 The conceptual scope of the problem is illustrated in Fig. 1, which summarises the functional elements of a  
102 force-feedback inertial sensor and their interactions. Within this framework, design requirements are not  
103 treated as independent specifications but as coupled constraints that jointly define the admissible design space.

104 The primary requirement considered in this work is the attainment of ultra-low self-noise levels over a broad  
105 frequency band spanning the ultra-low-frequency (ULF) regime to the classical broadband (BB) seismic band.

106 Such performance is essential for a wide range of geoscientific applications, including broadband seismology,  
107 gravimetry, and long-term environmental monitoring, where weak ground motions must be resolved across  
108 several decades in frequency (Collette et al., 2012; Carter et al., 2024).

109 A second key requirement concerns dynamic range and saturation behaviour. Ultra-low-noise operation must  
110 coexist with the capability to accommodate large transient signals without loss of linearity, control stability, or  
111 actuator authority (Sider et al., 2023). In force-feedback architectures, this requirement couples mechanical

12 design parameters, actuation strength, and control loop characteristics, precluding their independent  
13 optimisation (Zhao et al., 2022).

14 Additional constraints arise from digital acquisition and system-level resources, including power consumption,  
15 telemetry bandwidth, and data resolution, particularly in distributed or urban seismic monitoring

16 configurations based on compact MEMS instrumentation (D'Alessandro et al., 2014). Finite analog-to-digital  
17 converter (ADC) resolution, clock jitter, and digital signal processing limitations introduce noise contributions  
18 that may dominate the self-noise spectrum over specific frequency ranges, particularly at higher frequencies.

19 These effects must therefore be incorporated explicitly into the design formulation rather than treated as  
20 secondary implementation details (El-Sheimy et al., 2020; Ubezio et al., 2023).

21 Finally, the design requirements implicitly assume a set of environmental and operational conditions, including  
22 mechanical coupling to the ground, thermal stability, and station infrastructure. While these factors are not  
23 modelled explicitly in the present framework, they define the operating context within which the sensor is  
24 expected to meet its performance objectives and delimit the interpretation of the resulting performance bounds.

25 On the basis of the above requirements, the design problem is formulated as follows: given a target sensitivity  
26 spectrum, a frequency band of interest, and a set of implementation constraints, determine whether a physically  
27 realisable inertial sensor architecture can achieve the desired performance and identify the dominant  
28 mechanisms limiting that performance.

29 A central aspect of this formulation is the explicit separation between fundamental physical limits, such as  
30 thermal noise associated with mechanical dissipation, and implementation-dependent limits arising from  
31 readout electronics, actuation mechanisms, feedback control, and digital acquisition. This distinction is  
32 essential for meaningful interpretation of noise budgets and for guiding design decisions toward genuinely  
33 performance-limiting components rather than secondary contributors (Collette et al., 2012; Maculotti et al.,  
34 2024).

35 The sensor is modelled as a linear, time-invariant system operating around a stable equilibrium point. Its  
36 behaviour is described through transfer functions linking ground acceleration to the measured output quantity.  
37 Nonlinear effects such as actuator saturation, hysteresis, and large-amplitude geometric nonlinearities are  
38 neglected. These assumptions are standard in the analysis of ultra-low-noise inertial sensors and are justified  
39 when the focus is on noise-limited performance under nominal operating conditions (Carter et al., 2024).

ha formattato: Colore carattere: Testo 1

140 Within this framework, the observable of interest is the output acceleration estimate, whose power spectral  
141 density is determined by the combined effect of the sensor dynamics and all internal noise sources propagated  
142 through the system. The design objective is therefore the optimisation of the total self-noise spectrum, subject  
143 to causality, stability, and realisability constraints, rather than the minimisation of individual noise sources in  
144 isolation.

145 The formulation adopted here deliberately excludes experimental calibration data and site-specific noise  
146 conditions. This choice reflects the intended role of the framework as a design-stage and feasibility-assessment  
147 tool, rather than as a post-deployment diagnostic method. While this limits direct comparison with specific  
148 instruments, it enables the identification of general trends, trade-offs, and performance bounds that are  
149 transferable across sensor classes and deployment scenarios (Wright and Davidson, 2024; Ríos et al., 2020).

150 Model parameters, including mechanical damping and electronic noise levels, are assumed to be characterised  
151 by probability distributions reflecting their uncertainty. The systematic propagation of these uncertainties  
152 through the digital-twin framework is addressed in subsequent sections. The implications of these assumptions,  
153 and their potential impact on real-world performance, are discussed in Section 8.

### 156 **3. Digital-twin architecture and causal modeling**

157 The digital twin developed in this study is conceived as a physics-based, causal, and uncertainty-aware  
158 representation of an ultra-low-noise inertial sensor, explicitly designed to support metrological analysis and  
159 design-stage optimisation. Unlike generic simulation models or reduced-order representations, the proposed  
160 digital twin integrates mechanical dynamics, transduction, actuation, control, and digital acquisition within a  
161 unified framework that preserves physical causality and realisability.

162 A frequency-domain representation of the digital-twin response is shown in Fig. 2, illustrating the effect of  
163 force-feedback control on the system dynamics. This architecture reflects the functional decomposition of a  
164 force-feedback inertial sensor and provides the basis for subsequent noise propagation and performance  
165 analysis. In particular, Fig. 2(a) compares the open-loop mechanical response with the closed-loop response  
166 obtained under force-feedback control. The open-loop configuration exhibits a pronounced resonance at the  
167 natural frequency, whereas the closed-loop system suppresses this resonance and reduces proof-mass motion

168 over a broad frequency band. Fig. 2(b) shows the corresponding force-balance transfer function, highlighting  
169 how the feedback force tracks the inertial force at low frequencies and progressively rolls off at higher  
170 frequencies due to the finite bandwidth of the control loop.

171 The mechanical subsystem is modelled as a single-degree-of-freedom inertial plant characterised by an  
172 effective mass, elastic stiffness, and dissipative damping. This representation captures the dominant dynamics  
173 governing the sensor response in the frequency range of interest and is commonly adopted in the analysis of  
174 broadband and ultra-low-noise inertial sensors (Collette et al., 2012; Carter et al., 2024).

175 The validity of the single-degree-of-freedom (SDOF) approximation is restricted to the frequency range in  
176 which the fundamental mode dominates the mechanical response. In practice, this corresponds to frequencies  
177 sufficiently below the first higher-order structural resonance of the sensor assembly, where multi-mode effects  
178 and internal deformation of the mechanical structure can be neglected (Collette et al., 2012).

179 At very low frequencies, additional effects such as tilt coupling, foundation compliance, and environmental  
180 interactions may introduce deviations from the idealised inertial response. These effects are not explicitly  
181 modelled in the present framework and therefore delimit the lower bound of applicability of the SDOF  
182 representation.

183 The model further assumes rigid coupling between the sensor frame and the ground, negligible rotational  
184 degrees of freedom, and operation in the linear regime around a stable equilibrium configuration. Under these  
185 conditions, the SDOF approximation provides an accurate and physically consistent description of the  
186 dominant sensor dynamics relevant for noise-limited performance analysis.

187 Thermal noise associated with mechanical dissipation is treated as an intrinsic property of the plant and  
188 constitutes a fundamental performance limit. The mechanical model is assumed to operate in the linear regime  
189 around a stable equilibrium point, and temperature is treated as a stationary parameter. Spatially distributed  
190 modes, geometric nonlinearities, and thermoelastic coupling effects are neglected, an assumption justified  
191 when focusing on noise-limited performance well below structural resonance frequencies.

192 The transduction stage converts the mechanical state of the plant into an electrical signal. The digital twin  
193 represents this stage through a linear gain and an additive readout noise term, which may encompass optical,  
194 capacitive, or electromagnetic sensing mechanisms depending on the sensor implementation. This abstraction  
195 allows the framework to remain agnostic with respect to the specific readout technology while retaining its

196 metrological relevance. Compact interferometric readout implementations have recently been integrated in  
197 suspended interferometers, providing practical benchmarks for low-noise readout assumptions (Carter et al.,  
198 2025; Mitchell et al., 2025).

199 Readout noise is explicitly modelled as a stochastic process whose spectral characteristics can be prescribed  
200 or parameterised based on design assumptions. This representation is consistent with recent advances in ultra-  
201 low-noise front-end electronics for inertial sensors, where circuit-level optimisation plays a critical role in  
202 approaching fundamental sensitivity limits (Chen et al., 2024). This approach is consistent with modern inertial  
203 sensor analyses, where readout noise often dominates the self-noise spectrum outside the thermal-noise-limited  
204 band (Zhao et al., 2022; Carter et al., 2024).

205 Force-feedback actuation is incorporated into the digital twin to stabilise the mechanical plant and to linearise  
206 the sensor response. The actuation subsystem is represented by a causal transfer function linking the control  
207 signal to an applied force on the mechanical mass. Actuator noise and finite authority are treated as  
208 implementation-dependent limitations and are included explicitly in the model.

209 The control architecture is described by a stabilising controller acting on the measured output. Particular care  
210 is taken to ensure that the closed-loop system satisfies causality and stability constraints, as these conditions  
211 directly influence noise propagation and achievable performance. Non-causal inversions or idealised feedback  
212 laws are deliberately avoided, in contrast to some analytical treatments that neglect realisability constraints,  
213 often relying on idealised or non-causal representations of system transfer functions (Oppenheim and Schaffer,  
214 2010; Bendat and Piersol, 2010).

215 The final stage of the digital twin represents the digital acquisition process, including analog-to-digital  
216 conversion, finite resolution, and timing uncertainty. Quantisation noise and clock jitter are modelled explicitly  
217 and propagated through the system in subsequent analyses. This treatment reflects the growing recognition  
218 that digital acquisition can impose dominant performance limits in ultra-low-noise sensors, particularly at  
219 higher frequencies or under stringent power constraints (El-Sheimy et al., 2020; Ubezio et al., 2023).

220 Discretisation effects are treated consistently with the causal structure of the system. Continuous-time transfer  
221 functions are mapped to their discrete-time counterparts using stable and physically meaningful  
222 transformations. This ensures that the digital twin remains a faithful representation of a realisable sensor  
223 system rather than an idealised mathematical construct. Open-source simulation toolchains widely used in



251 twin and defines the methodology used to propagate uncertainty from individual noise sources to the total self-  
252 noise spectrum.

253 A schematic overview of the noise budget and its decomposition into individual contributions is shown in Fig.  
254 3, which provides a graphical representation of the formalism developed below.

255 Starting from the equation of motion introduced in Eq. (1), the system is transformed into the frequency domain  
256 under the assumption of linear, time-invariant dynamics. Taking the Fourier transform of Eq. (1) and using the  
257 standard correspondence  $d/dt \rightarrow i\omega$ , the equation of motion can be written in the frequency domain as

258

259  ~~$(-m\omega^2 + ic\omega + k)X(\omega) = -mA_g(\omega) + F_{fb}(\omega);$~~

260

262  $(-m\omega^2 + ic\omega + k)X(\omega) = -mA_g(\omega) + F_{fb}(\omega). \quad (2)$

261

263 Denoting Fourier-transformed quantities by capital letters, the relative displacement  $X(\omega)$  of the inertial mass  
264 can be written as

265

267  ~~$X(\omega) = \frac{-mA_g(\omega) + F_{fb}(\omega)}{k - m\omega^2 + ic\omega};$~~   $X(\omega) = \frac{-mA_g(\omega) + F_{fb}(\omega)}{k - m\omega^2 + ic\omega}, \quad (3)$

266

268 where  $A_g(\omega)$  is the ground acceleration spectrum and  $F_{fb}(\omega)$  represents the feedback force in the frequency  
269 domain. Equation (23) defines the mechanical susceptibility of the plant and provides the basis for constructing  
270 the transfer functions linking each noise source to the sensor output.

271 In a force-feedback configuration, the measured output is typically proportional to an estimate of the ground  
272 acceleration derived from the control signal and the plant response. The digital twin represents this relationship  
273 through a set of causal transfer functions  $T_{gA}(\omega)$ , each associated with a specific noise source  $q$ .

274 The total self-noise of the sensor is defined as the output noise spectrum obtained in the absence of ground  
275 motion, i.e. for  $A_g(\omega) = 0$ . Under the assumption of linearity and mutual incoherence of the noise sources,  
276 the total output power spectral density can be expressed as the sum of the individual contributions propagated  
277 through their respective transfer functions. This follows from standard results in linear systems theory, where

ha formattato: Colore carattere: Testo 1

ha formattato: Colore carattere: Testo 1

ha formattato: Colore carattere: Testo 1

ha formattato: Colore carattere: Testo 1

ha formattato: Colore carattere: Testo 1

ha formattato: Colore carattere: Testo 1

ha formattato: Colore carattere: Testo 1

ha formattato: Colore carattere: Testo 1

ha formattato: Colore carattere: Testo 1

ha formattato: Colore carattere: Testo 1

ha formattato: Colore carattere: Testo 1

ha formattato: Colore carattere: Testo 1

ha formattato: Colore carattere: Testo 1

ha formattato: Colore carattere: Testo 1

ha formattato: Colore carattere: Testo 1

ha formattato: Colore carattere: Testo 1

ha formattato: Colore carattere: Testo 1

278 each noise source is treated as an independent stochastic input and its contribution is weighted by the squared  
279 magnitude of the corresponding transfer function (e.g., Bendat and Piersol, 2010; El-Sheimy et al., 2020).  
280 Under this condition, the output acceleration noise power spectral density (PSD) can be expressed as the  
281 incoherent sum of the contributions from all internal noise sources,

282

$$284 \quad S_{a,\text{self}}(\omega) = \sum_q |T_q(\omega)|^2 S_q(\omega), \quad (3) \quad S_{a,\text{self}}(\omega) = \sum_q |T_q(\omega)|^2 S_q(\omega), \quad (4)$$

283

285 where  $S_q(\omega)$  denotes the PSD of the  $q$ -th noise source and  $T_q(\omega)$  is the corresponding transfer function from  
286 that source to the output acceleration estimate. Equation (34) constitutes the central metrological relation of  
287 the framework and formalises the noise-budget decomposition illustrated in Fig. 3.

288 The noise sources considered in this work include: (i) thermal (Brownian) noise associated with mechanical  
289 dissipation, (ii) readout noise originating from the transduction stage, (iii) actuation noise introduced by the  
290 force-feedback mechanism, (iv) digital acquisition noise, including quantisation and timing uncertainty.

291 Similar PSD-based and variance-based approaches for inertial sensor self-noise characterization have been  
292 previously applied to MEMS accelerometric systems (D'Alessandro et al., 2017).

293 Thermal noise associated with mechanical damping represents a fundamental physical limit that cannot be  
294 reduced without modifying the underlying dissipation mechanisms. Its contribution is governed by the  
295 fluctuation–dissipation theorem and depends on temperature, damping, and mechanical susceptibility (Collette  
296 et al., 2012).

297 In contrast, readout, actuation, and digital acquisition noises are implementation-dependent and reflect  
298 technological and design choices. Their relative importance varies across frequency and design parameter  
299 space, and they often dominate the self-noise spectrum outside the thermal-noise-limited band (Zhao et al.,  
300 2022; Carter et al., 2024). The explicit separation between these two classes of noise sources is essential for  
301 interpreting metrological bounds and guiding effective design optimisation.

302 All noise sources and model parameters entering Eq. (34) are subject to uncertainty arising from manufacturing  
303 tolerances, environmental variability, and modelling assumptions. Within the digital-twin framework, these  
304 uncertainties are represented through probability distributions assigned to the relevant parameters.

ha formattato: Colore carattere: Testo 1

ha formattato: Colore carattere: Testo 1

ha formattato: Colore carattere: Testo 1

ha formattato: Colore carattere: Testo 1

ha formattato: Colore carattere: Testo 1

ha formattato: Colore carattere: Testo 1

ha formattato: Colore carattere: Testo 1

ha formattato: Colore carattere: Testo 1

ha formattato: Colore carattere: Testo 1

ha formattato: Colore carattere: Testo 1

305 Uncertainty propagation is performed by evaluating the statistical distribution of the self-noise spectrum  
306 resulting from Eq. (34), given the distributions of  $S_{\mu}(\omega)$  and the parameters defining  $T_{\mu}(\omega)$ . This approach is  
307 consistent with recent developments in digital twin-based uncertainty mapping and error propagation in  
308 metrological systems, where spatial and parametric uncertainties are explicitly quantified within virtual  
309 representations (Sepahi-Boroujeni and Khameneifar, 2024). This approach enables the estimation of  
310 confidence intervals on the predicted self-noise and provides a quantitative measure of robustness with respect  
311 to parameter variability, in line with modern metrological digital-twin concepts (Scholz et al., 2022; Wübbeler  
312 et al., 2022; Wright and Davidson, 2024; Maculotti et al., 2024).

313 Parameter correlations are neglected unless explicitly stated. While this assumption may not hold in all  
314 practical implementations, it allows the identification of dominant uncertainty drivers and represents a  
315 reasonable first-order approximation for design-stage analysis.

316 The noise modeling framework assumes linearity, stationarity, and mutual incoherence of the noise sources.  
317 Cross-correlations between noise processes and non-stationary effects are not considered. These assumptions  
318 are standard in inertial sensor metrology and are justified when the objective is to characterise noise-limited  
319 performance under nominal operating conditions.

320 The implications of these assumptions, and their potential impact on real-world sensor behaviour, are discussed  
321 in Section 8.

322

323

## 324 5. Spectral performance and self-noise regimes

325 This section analyses the spectral performance predicted by the digital twin and characterises the resulting self-  
326 noise in terms of dominant noise regimes across frequency. The objective is to translate the metrological  
327 formulation introduced in Section 4 into physically interpretable performance metrics that are directly relevant  
328 for sensor design.

329 A representative example of the self-noise spectrum and its decomposition into individual contributions is  
330 shown in Fig. 4, which illustrates how fundamental and implementation-dependent noise sources shape the  
331 achievable performance across the frequency band of interest.

ha formattato: Colore carattere: Testo 1

ha formattato: Colore carattere: Testo 1

ha formattato: Colore carattere: Testo 1

ha formattato: Colore carattere: Testo 1

ha formattato: Colore carattere: Testo 1

ha formattato: Colore carattere: Testo 1

ha formattato: Colore carattere: Testo 1

332 The parameter ranges adopted in this analysis, including mechanical properties, damping ratios, and  
 333 representative noise levels, are consistent with those reported for state-of-the-art broadband and ultra-low-  
 334 noise inertial sensors (e.g., Collette et al., 2012; Carter et al., 2024), ensuring that the simulated performance  
 335 remains representative of physically achievable instrument designs.

336 The total self-noise spectrum  $S_{a,\text{self}}(\omega)$ , defined in Eq. (34), typically exhibits distinct frequency-dependent  
 337 behaviours governed by the interplay between mechanical susceptibility and noise transfer functions. Of  
 338 particular interest is the presence of noise plateaus, i.e. frequency intervals over which the self-noise remains  
 339 approximately constant.

340 To formalise this concept, the acceleration self-noise amplitude spectral density (ASD) is defined as

341

342 ~~$$N_a(\omega) = \sqrt{S_{a,\text{self}}(\omega)} \quad (4)$$~~ 
$$N_a(\omega) = \sqrt{S_{a,\text{self}}(\omega)} \quad (5)$$

343

344 A plateau region is identified when the logarithmic slope of  $N_a(\omega)$  with respect to frequency satisfies

345

346 ~~$$\left| \frac{d \log N_a(\omega)}{d \log \omega} \right| < \varepsilon \quad (5)$$~~ 
$$\left| \frac{d \log N_a(\omega)}{d \log \omega} \right| < \varepsilon \quad (6)$$

347

348 where  $\varepsilon$  is a small threshold chosen to discriminate between flat and sloped spectral behaviour. While the  
 349 precise value of  $\varepsilon$  is application-dependent, the qualitative identification of plateau regions is robust with  
 350 respect to reasonable threshold variations.

351 Plateaus are of particular metrological relevance because they define frequency bands in which the sensor  
 352 sensitivity is maximised and least sensitive to modelling uncertainties.

353 Across the full frequency band, different noise sources dominate the self-noise spectrum. At low frequencies,  
 354 the response is typically governed by thermal noise associated with mechanical damping, reflecting the  
 355 fundamental limit imposed by dissipation mechanisms. In intermediate frequency ranges, readout or actuation  
 356 noise may dominate, depending on the chosen transduction and control architecture. At higher frequencies,  
 357 digital acquisition noise, including quantisation and timing uncertainty, often becomes the limiting factor.

- ha formattato: Colore carattere: Testo 1
- ha formattato: Colore carattere: Testo 1
- ha formattato: Colore carattere: Testo 1
- ha formattato: Colore carattere: Testo 1

- ha formattato: Colore carattere: Testo 1

- ha formattato: Colore carattere: Testo 1
- ha formattato: Colore carattere: Testo 1
- ha formattato: Colore carattere: Testo 1
- ha formattato: Colore carattere: Testo 1

358 These dominant noise regimes are identified by comparing the individual terms in Eq. (34) and determining,  
359 at each frequency, the noise source contributing the largest fraction to  $S_{a,self}(\omega)$ . This regime-based  
360 interpretation is illustrated in Fig. 4, where transitions between thermal-limited and implementation-limited  
361 behaviour are clearly visible.

362 The identification of dominant regimes is a consolidated result, as it directly follows from the noise budget  
363 formalism and does not depend on subjective interpretation. In contrast, the precise frequency boundaries  
364 between regimes should be regarded as model-dependent and may shift as design parameters or uncertainty  
365 assumptions are varied.

366 A central outcome of the spectral analysis is the explicit comparison between the total self-noise and the  
367 thermal noise floor. The ratio

368

370

$$R(\omega) = \frac{S_{a,self}(\omega)}{S_{a,th}(\omega)} \quad (6) \quad R(\omega) = \frac{S_{a,self}(\omega)}{S_{a,th}(\omega)} \quad (7)$$

369

371 provides a frequency-dependent measure of the margin to the thermal limit, where  $S_{a,th}(\omega)$  denotes the thermal  
372 noise contribution. Values of  $R(\omega)$  close to unity indicate near-thermal-limited performance, whereas larger  
373 values highlight the dominance of implementation-dependent noise sources.

374 This ratio constitutes a key diagnostic metric for sensor design, as it directly indicates whether further  
375 performance improvements require fundamental changes to the mechanical plant or, alternatively,  
376 technological improvements in readout, actuation, or digital acquisition. The interpretation of  $R(\omega)$  across  
377 frequency is illustrated in Fig. 4, where near-thermal and implementation-limited bands can be clearly  
378 distinguished.

379 The spectral features identified in this section are a direct consequence of the causal structure of the digital  
380 twin and the noise modeling assumptions introduced in Section 4. While the existence of plateaus and dominant  
381 noise regimes is a robust qualitative result, their quantitative characteristics depend on model parameters and  
382 uncertainty distributions.

383 Nonlinear effects, cross-correlations between noise sources, and non-stationary behaviour are not considered  
384 in this analysis. These factors may alter the detailed spectral structure in real instruments, particularly under

ha formattato: Colore carattere: Testo 1

ha formattato: Colore carattere: Testo 1

ha formattato: Colore carattere: Testo 1

ha formattato: Colore carattere: Testo 1

ha formattato: Colore carattere: Testo 1

ha formattato: Colore carattere: Testo 1

ha formattato: Colore carattere: Testo 1

ha formattato: Colore carattere: Testo 1

ha formattato: Colore carattere: Testo 1

385 extreme operating conditions. Nevertheless, the regime-based interpretation presented here provides a  
 386 physically meaningful and practically useful framework for guiding sensor design.

387  
 388

### 389 6. Crossover frequencies and design trade-offs

390 While the identification of dominant noise regimes provides a qualitative understanding of sensor performance,  
 391 practical design decisions require quantitative metrics capable of capturing transitions between regimes and  
 392 their dependence on key design parameters. In this section, such metrics are introduced through the concept of  
 393 crossover frequencies, which mark the boundaries between noise-dominated regimes and provide a compact  
 394 description of performance trade-offs.

395 A representative mapping of crossover frequencies and dominant regimes in the design parameter space is  
 396 shown in Fig. 6, which synthesises the spectral analyses discussed in the previous section.

397 For any pair of noise sources  $q_1$  and  $q_2$ , a crossover frequency  $\omega_c^{(q_1, q_2)}$  is defined as the solution of

398

400  ~~$|T_{q_1}(\omega_c)|^2 S_{q_1}(\omega_c) = |T_{q_2}(\omega_c)|^2 S_{q_2}(\omega_c)$~~  (7)  ~~$|T_{q_1}(\omega_c)|^2 S_{q_1}(\omega_c) = |T_{q_2}(\omega_c)|^2 S_{q_2}(\omega_c)$~~

399

401 i.e. the frequency at which the contributions of the two noise sources to the total self-noise spectrum are equal.

402 Below and above this frequency, the dominant contribution switches from one noise source to the other.

403 In practice, the most relevant crossover frequencies involve transitions between thermal noise and  
 404 implementation-dependent noise sources, such as readout or digital acquisition noise. These transitions  
 405 delineate frequency intervals in which further performance improvements require fundamentally different  
 406 design strategies.

407 Building on the plateau definition introduced in Section 5, the near-plateau bandwidth is defined as the  
 408 frequency interval over which the self-noise remains within a prescribed margin of the minimum achievable  
 409 level. Formally, this interval is given by

410

412  ~~$N_a(\omega) \leq (1 + \delta) N_{a, \min}$~~  (8)  ~~$N_a(\omega) \leq (1 + \delta) N_{a, \min}$~~  (9)

411

- ha formattato: Colore carattere: Testo 1
- ha formattato: Colore carattere: Testo 1
- ha formattato: Colore carattere: Testo 1
- ha formattato: Colore carattere: Testo 1
- ha formattato: Colore carattere: Testo 1
- ha formattato: Colore carattere: Testo 1
- ha formattato: Colore carattere: Testo 1
- ha formattato: Colore carattere: Testo 1
- ha formattato: Colore carattere: Testo 1
- ha formattato: Colore carattere: Testo 1
- ha formattato: Colore carattere: Testo 1
- ha formattato: Colore carattere: Testo 1

ha formattato: Colore carattere: Testo 1

413 where  $N_{g,\min}$  is the minimum value of the self-noise ASD and  $\delta$  is a tolerance parameter. The near-plateau  
414 bandwidth provides a concise metric for assessing the usable frequency range over which the sensor operates  
415 close to its optimal sensitivity.

416 As illustrated in Fig. 6, this bandwidth is strongly dependent on implementation parameters such as ADC  
417 resolution and control-loop design, and it often represents a more informative performance metric than the  
418 absolute minimum noise level alone.

419 The crossover frequencies and near-plateau bandwidth jointly define a design trade-off space in which  
420 improvements along one dimension may degrade performance along another. For example, increasing digital  
421 resolution can extend the near-plateau bandwidth toward higher frequencies but may impose penalties in power  
422 consumption or system complexity. Conversely, modifying mechanical damping may shift thermal-to-readout  
423 crossover frequencies at the expense of increased sensitivity to environmental perturbations.

424 The regime maps shown in Fig. 6 summarise these trade-offs by identifying, for each region of the parameter  
425 space, the noise source that ultimately limits performance. These maps constitute a consolidated result, as they  
426 are derived directly from the noise-budget formalism and the causal structure of the digital twin. However, the  
427 precise boundaries between regimes should be interpreted as model-dependent, reflecting assumptions on  
428 parameter uncertainty and noise spectra.

429 From a design perspective, crossover-based metrics provide actionable guidance by indicating whether further  
430 optimisation efforts should focus on fundamental mechanical improvements or on technological enhancements  
431 in readout, actuation, or digital acquisition. In this sense, crossover frequencies act as decision thresholds  
432 separating regimes where different design strategies are effective.

433 It is important to note that crossover frequencies are not intrinsic properties of the sensor but emerge from the  
434 interaction between physical dynamics and implementation choices. As such, they should be interpreted within  
435 the context of the assumed operating conditions and uncertainty model. The broader implications of this  
436 dependence are discussed in Section 8.

437

438

## 439 7. Performance metrics and design optimization

ha formattato: Colore carattere: Testo 1

ha formattato: Colore carattere: Testo 1

ha formattato: Colore carattere: Testo 1

440 The spectral analyses and crossover-based diagnostics introduced in the previous sections provide detailed  
 441 insight into the noise-limited behaviour of ultra-low-noise inertial sensors. For design purposes, however, it is  
 442 often desirable to condense this information into a limited set of performance metrics that can guide  
 443 optimisation decisions and enable comparisons between alternative architectures. This section introduces such  
 444 metrics and illustrates their role within the digital-twin framework.

445 A synthesis of the performance metrics discussed below and their dependence on key design parameters is  
 446 shown in Fig. 7, which summarises the design space explored in this study.

447 A primary metric is the minimum self-noise level, defined as

448

$$450 \quad \cancel{N_{a,\min} = \min_{\omega} N_a(\omega), \quad (9)} \quad N_{a,\min} = \min_{\omega} N_a(\omega), \quad (10)$$

449

451 where  $N_a(\omega)$  is the self-noise ASD defined in Eq. (45). While  $N_{a,\min}$  provides a compact measure of ultimate  
 452 sensitivity, it does not capture the frequency extent over which this sensitivity is achieved. As such, it should  
 453 not be used in isolation to rank sensor designs.

454 Complementary information is provided by the near-plateau bandwidth introduced in Section 6, which  
 455 quantifies the usable frequency interval over which the self-noise remains close to its minimum value.

456 Together, these two metrics define a sensitivity–bandwidth trade-off that is central to sensor design.

457 To assess how closely a given design approaches the fundamental thermal noise limit, the margin to the thermal  
 458 bound is evaluated using the ratio defined in Eq. (67). For practical design optimisation, a scalar metric can be  
 459 introduced by averaging this ratio over a frequency interval of interest  $[\omega_1, \omega_2]$ .

460

$$462 \quad \cancel{\bar{R} = \frac{1}{\omega_2 - \omega_1} \int_{\omega_1}^{\omega_2} \frac{S_{a,\text{self}}(\omega)}{S_{a,\text{th}}(\omega)} d\omega, \quad (10)} \quad \bar{R} = \frac{1}{\omega_2 - \omega_1} \int_{\omega_1}^{\omega_2} \frac{S_{a,\text{self}}(\omega)}{S_{a,\text{th}}(\omega)} d\omega. \quad (11)$$

461

463 Values of  $\bar{R}$  close to unity indicate near-thermal-limited performance over the selected band, whereas larger  
 464 values highlight the dominance of implementation-dependent noise sources. This metric is particularly useful

ha formattato: Colore carattere: Testo 1

ha formattato: Colore carattere: Testo 1

ha formattato: Colore carattere: Testo 1

ha formattato: Colore carattere: Testo 1

ha formattato: Colore carattere: Testo 1

ha formattato: Colore carattere: Testo 1

ha formattato: Colore carattere: Testo 1

ha formattato: Colore carattere: Testo 1

ha formattato: Colore carattere: Testo 1

ha formattato: Colore carattere: Testo 1

ha formattato: Colore carattere: Testo 1

ha formattato: Colore carattere: Testo 1

ha formattato: Colore carattere: Testo 1

ha formattato: Colore carattere: Testo 1

ha formattato: Colore carattere: Testo 1

ha formattato: Colore carattere: Testo 1

ha formattato: Colore carattere: Testo 1

465 for identifying whether further optimisation efforts should focus on mechanical design or on technological  
466 improvements in readout and digital acquisition.

467 Beyond absolute performance, robustness with respect to parameter uncertainty constitutes a critical aspect of  
468 sensor design. Within the digital-twin framework, robustness is assessed by analysing the variability of the  
469 performance metrics introduced above under the assumed parameter uncertainty distributions.

470 Designs that achieve marginally lower self-noise but exhibit strong sensitivity to parameter variations may be  
471 less desirable than slightly noisier but more robust configurations. This consideration is especially relevant for  
472 long-term geoscientific deployments, where environmental variability and ageing effects can significantly  
473 impact performance (Wright and Davidson, 2024).

474 The optimisation strategy adopted here therefore prioritises uncertainty-aware performance, favouring regions  
475 of the design space in which sensitivity, bandwidth, and robustness are jointly optimised. The regime maps  
476 shown in Fig. 7 illustrate how such regions can be identified and compared across alternative design choices.

477 Within the proposed framework, design optimisation proceeds iteratively. Initial design choices define a  
478 candidate digital twin, whose performance metrics are evaluated using the methods described above. Identified  
479 bottlenecks then guide targeted modifications to mechanical parameters, control architecture, or digital  
480 acquisition settings, and the analysis is repeated until the desired performance objectives are met.

481 This optimisation process is methodologically consolidated, as it relies on physically interpretable metrics  
482 derived directly from the causal digital twin. At the same time, specific optimisation outcomes remain context-  
483 dependent, reflecting application-specific requirements and constraints. The broader implications of this  
484 balance between generality and specificity are discussed in Section 8.

485

486

## 487 **8. Discussion**

488 Recent advances in digital-twin methodologies for metrology have emphasised the importance of uncertainty  
489 quantification, traceability, and physically consistent virtual experimentation (Wright and Davidson, 2024;  
490 Maculotti et al., 2024). The present framework aligns with these developments by extending such principles  
491 to force-feedback inertial sensors and explicitly incorporating causality constraints within the modeling  
492 architecture.

493 This section discusses the implications of the proposed causal and uncertainty-aware digital-twin framework,  
494 placing the results presented in Sections 4–7 in a broader methodological and instrumental context. The  
495 discussion focuses on the generality of the approach, its limitations, and its relevance for the design of ultra-  
496 low-noise geoscientific inertial sensors.

497 A conceptual synthesis of the workflow and its role in guiding design decisions is illustrated in Fig. 8, which  
498 integrates the individual analysis steps into a unified methodological framework.

499 A key outcome of this study is that enforcing physical causality and realisability constraints at the digital-twin  
500 level is essential for obtaining meaningful metrological predictions. Non-causal or idealised representations  
501 may lead to overly optimistic noise estimates and obscure the distinction between fundamental and  
502 implementation-dependent limits. (Wright and Davidson, 2024; Maculotti et al., 2024).

503 The practical relevance of these metrics can be illustrated through representative design scenarios based on  
504 Figs. 4–7.

505 In a first scenario, consider a design operating close to the thermal noise limit over a restricted frequency band,  
506 as indicated by  $R(\omega) \approx 1$  in Fig. 4. In this regime, further improvements in sensitivity cannot be achieved  
507 through readout or digital optimisation alone, and require modifications of the mechanical plant, such as  
508 reducing dissipation or increasing effective mass. This identifies the thermal-to-readout crossover as a key  
509 decision threshold between mechanical and electronic optimisation strategies.

510 In a second scenario, Fig. 6 shows that increasing ADC resolution shifts the crossover between digital and  
511 actuation noise toward higher frequencies, effectively extending the near-plateau bandwidth. However, as  
512 illustrated in Fig. 7, this improvement saturates beyond a certain ENOB (Effective Number of Bits), beyond  
513 which actuator or readout noise becomes dominant. This demonstrates that digital optimisation alone cannot  
514 ensure broadband performance gains.

515 A third scenario concerns the role of damping, as shown in Fig. 5. Variations in damping primarily affect low-  
516 frequency performance through their impact on thermal noise and feedback dynamics, while high-frequency  
517 behaviour remains largely unchanged. This indicates that mechanical and digital parameters act on distinct  
518 spectral regions, enabling targeted and decoupled optimisation strategies.

519 The performance metrics introduced in Sections 6 and 7 provide a compact representation of complex spectral  
520 information and facilitate comparison between alternative sensor architectures. In particular, crossover

521 frequencies and near-plateau bandwidths offer actionable indicators of where design effort is most effectively  
522 directed.

523 The proposed framework can be further contextualised by comparison with conventional sensor design  
524 methodologies. Traditional noise budgeting approaches typically evaluate individual noise contributions  
525 independently and combine them a posteriori, often neglecting system-level coupling effects introduced by  
526 feedback control and digital acquisition. While such approaches are effective for first-order performance  
527 estimation, they may lead to inconsistencies when applied to closed-loop architectures, where transfer  
528 functions are inherently interdependent.

529 Simplified digital twin models, on the other hand, often represent individual subsystems or rely on non-causal  
530 inversions to estimate idealised performance limits. Although computationally efficient, these formulations  
531 may overlook constraints imposed by causality and realisability, leading to optimistic predictions of achievable  
532 sensitivity.

533 In contrast, the present framework enforces causal system dynamics at all stages and propagates all noise  
534 sources through a unified set of transfer functions, enabling a consistent system-level evaluation. The resulting  
535 performance metrics, including crossover frequencies (Eq. 78) and near-plateau bandwidth (Eq. 89), provide  
536 quantitative indicators that are not directly accessible through conventional noise budgeting approaches.

537 From a quantitative perspective, the ratio to the thermal limit (Eq. 67) and its band-averaged form (Eq. 101)  
538 enable a direct comparison between designs, while explicitly accounting for implementation-dependent  
539 constraints. These metrics highlight how different design strategies shift regime boundaries rather than  
540 uniformly improving performance, an effect that is not captured by traditional component-wise optimisation.

541 This comparison indicates that the main advantage of the proposed digital twin lies not in redefining  
542 fundamental limits, but in providing a physically consistent and uncertainty-aware framework to approach  
543 them in a controlled and interpretable manner.

544 A schematic comparison of the different methodological approaches is provided in Fig. 910, highlighting how  
545 the proposed framework enables physically consistent and uncertainty-aware system-level design.

546 The regime maps derived from these metrics should be interpreted as decision-support tools rather than as  
547 absolute performance predictors. While the existence of distinct noise-dominated regimes is a robust outcome  
548 of the noise-budget formalism, the precise boundaries between regimes depend on modelling assumptions and

ha formattato: Colore carattere: Testo 1

ha formattato: Colore carattere: Testo 1

ha formattato: Colore carattere: Testo 1

ha formattato: Colore carattere: Testo 1

ha formattato: Colore carattere: Testo 1

549 uncertainty characterisation. This sensitivity underscores the importance of uncertainty-aware optimisation  
550 strategies in sensor design.

551 Although the digital twin is formulated with force-feedback inertial sensors in mind, the underlying  
552 methodology is not restricted to a specific sensor type. The same framework can be adapted to other classes of  
553 geoscientific instruments, such as tiltmeters, gravimeters, or strain sensors, including atom-interferometry  
554 gravimeters demonstrated in harsh volcanic environments (Antoni-Micollier et al., 2022), provided that their  
555 dynamics can be represented within a linear, causal system framework.

556 The abstraction of transduction, actuation, and digital acquisition as modular subsystems facilitates such  
557 extensions and supports the development of sensor-specific digital twins within a common metrological  
558 structure. This generality is consistent with recent efforts to standardise digital-twin methodologies across  
559 measurement domains (Ríos et al., 2020; Ubezio et al., 2023).

560 Several limitations of the present framework should be acknowledged. First, the analysis assumes linearity,  
561 stationarity, and mutual incoherence of noise sources. While these assumptions are standard in inertial sensor  
562 metrology, they may be violated under extreme operating conditions or in the presence of strong environmental  
563 coupling.

564 Second, parameter uncertainties are treated as statistically independent unless explicitly stated. In real  
565 instruments, correlations between mechanical, electronic, and environmental parameters may exist and could  
566 affect uncertainty propagation. Incorporating such correlations would require additional modelling effort and  
567 data, which lies beyond the scope of the present study.

568 Finally, the framework does not incorporate site-specific noise conditions or experimental calibration data. As  
569 a result, the predicted performance should be interpreted as an intrinsic sensor capability rather than as a  
570 guarantee of field performance. This distinction is particularly important when comparing digital-twin  
571 predictions with observational data.

572 A further limitation of the present study is the lack of direct experimental validation against specific sensor  
573 prototypes. This reflects the intended role of the proposed digital twin as a design-stage and feasibility-  
574 assessment tool, rather than as a post-deployment calibration framework.

575 In this context, the objective is not to reproduce the performance of a particular instrument, but to provide a  
576 physically consistent and causality-constrained environment for exploring design trade-offs and identifying  
577 fundamental and implementation-dependent performance limits.

578 Nevertheless, the integration of the digital twin with experimental data represents a natural and important  
579 extension of the present work, as demonstrated by recent metrology-integrated digital twin frameworks that  
580 explicitly combine physical models with measurement data for validation and calibration purposes (Samadi et  
581 al., 2025). Future developments may include the use of laboratory or field measurements to calibrate model  
582 parameters, validate predicted self-noise spectra, and refine uncertainty distributions within a data-informed  
583 framework.

584 Despite these limitations, the proposed framework provides a solid foundation for future extensions. Potential  
585 developments include the incorporation of nonlinear effects, the integration of experimental calibration data  
586 to refine parameter distributions, and the coupling of the digital twin with real-time monitoring systems. Data-  
587 driven denoising approaches have also been explored for inertial sensors/accelerometers and may complement  
588 model-based digital twins (Yang et al., 2023).

589 Such extensions would further enhance the utility of digital twins as tools for both design-stage optimisation  
590 and operational performance assessment in geoscientific instrumentation.

591

592

## 593 **9. Conclusions**

594 This work introduces a causal and uncertainty-aware digital-twin framework for the design and metrological  
595 assessment of ultra-low-noise geoscientific inertial sensors. The framework integrates mechanical dynamics,  
596 force-feedback control, transduction, and digital acquisition within a physically realisable and causally  
597 consistent representation.

598 A central contribution is the formulation of a unified noise-budget model that distinguishes between  
599 fundamental thermal limits and implementation-dependent noise sources, enabling physically interpretable  
600 self-noise predictions and uncertainty-aware performance assessment.

601 The results demonstrate that enforcing causality and realisability is essential for obtaining reliable performance  
602 estimates, particularly in ultra-low-noise regimes where idealised formulations may lead to overly optimistic  
603 predictions.

604 Despite the simplifying assumptions adopted, the proposed framework provides a robust and extensible  
605 foundation for design-stage optimisation and virtual experimentation. Potential extensions include the  
606 incorporation of nonlinear effects, correlated uncertainties, and experimental calibration data.

607 Beyond inertial sensors, the methodology is readily transferable to other classes of geoscientific instruments,  
608 supporting the broader adoption of digital twins as design and decision-support tools in geoscientific  
609 instrumentation.

610

611

#### 612 **Competing interests:**

613 The authors declare that they have no conflict of interest

614

615

#### 616 **10. References**

617 Antoni-Micollier, L., *et al.* (2022). Detecting volcano-related underground mass changes with a quantum  
618 gravimeter. *Geophysical Research Letters*, 49, e2022GL097814. <https://doi.org/10.1029/2022GL097814>.

619  
620 Bai, W., Feng, W., Wang, P., Zhang, Z., and Zhao, G. (2025). Research on Interferometric Tilt Sensor for  
621 Vibration Isolation Platform. *Sensors*, 25(6), 1777. <https://doi.org/10.3390/s25061777>.

622  
623 Bendat, J. S., & Piersol, A. G. (2010). *Random Data: Analysis and Measurement Procedures* (4th ed.). Wiley.  
624 <https://doi.org/10.1002/9781118032428>.

625  
626 Brown, D. D., Jones, P., Rowlinson, S., Leavey, S., Green, A. C., Töyrä, D., and Freise, A. (2020). Pykat:  
627 Python package for modelling precision optical interferometers. *SoftwareX*, 12, 100613.  
628 <https://doi.org/10.1016/j.softx.2020.100613>

ha formattato: Colore carattere: Testo 1, Inglese (Stati Uniti)

ha formattato: Colore carattere: Testo 1

ha formattato: Colore carattere: Testo 1, Francese (Francia)

ha formattato: Colore carattere: Testo 1, Francese (Francia)

ha formattato: Colore carattere: Testo 1, Francese (Francia)

ha formattato: Colore carattere: Testo 1

ha formattato: Colore carattere: Testo 1, Inglese (Stati Uniti)

ha formattato: Colore carattere: Testo 1

629  
630  
631  
632  
633  
634  
635  
636  
637  
638  
639  
640  
641  
642  
643  
644  
645  
646  
647  
648  
649  
650  
651  
652  
653  
654  
655  
656

Carlin, *et al.* (2024). An interactive framework to support decision-making for Digital Twin design. *Journal of Industrial Information Integration*, 41, 100639. <https://doi.org/10.1016/j.jii.2024.100639>

Carter, J. J., Birckigt, P., Gerberding, O., and Koehlenbeck, S. M. (2024). High precision inertial sensors on a one inch diameter optic. *Scientific Reports*, 14. <https://doi.org/10.1038/s41598-024-68623-0>

ha formattato: Colore carattere: Testo 1  
ha formattato: Colore carattere: Testo 1

Carter, J. J., *et al.* (2025). Testing compact, fused silica resonator based inertial sensors in a gravitational wave detector prototype facility. *Classical and Quantum Gravity*, 42(18), 185001. <https://doi.org/10.1088/1361-6382/adff34>

Chen, Y., Liu, X., Wang, L., Yu, T., Wang, Z., Xue, K., Sui, Y., & Chen, Y. (2024). Research and optimization of high-performance front-end circuit noise for inertial sensors. *Sensors*, 24(3), 805. <https://doi.org/10.3390/s24030805>

ha formattato: Colore carattere: Testo 1, Inglese (Stati Uniti)  
ha formattato: Colore carattere: Testo 1

Collette, C., Janssens, S., Fernandez-Carmona, P., Artoos, K., Guinchard, M., Hauviller, C., and Preumont, A. (2012). Review: Inertial sensors for low-frequency seismic vibration measurement. *Bulletin of the Seismological Society of America*, 102(4), 1289–1300. <https://doi.org/10.1785/0120110223>

ha formattato: Colore carattere: Testo 1  
ha formattato: Tipo di carattere: Times New Roman, 11 pt

[D'Alessandro, A., and D'Anna, G. \(2013\). Suitability of low-cost three-axis MEMS accelerometers in strong-motion seismology: tests on the LIS331DLH \(iPhone\) accelerometer. \*Bulletin of the Seismological Society of America\*, 103\(5\), 2906–2913. <https://doi.org/10.1785/0120120287>](#)

[D'Alessandro, A., Vitale, G., Scudero, S., D'Anna, R., Passafiume, G., Greco, L., and Speciale, S. \(2017\). Characterization of MEMS accelerometer self-noise by means of PSD and Allan Variance analysis. In 2017 \*IEEE International Workshop on Advances in Sensors and Interfaces \(IWASI\)\*, 166–171. <https://doi.org/10.1109/IWASI.2017.7974238>](#)

657 [D'Alessandro, A., Luzio, D., and D'Anna, G. \(2014\). Urban MEMS based seismic network for post-earthquake](#)  
658 [rapid disaster assessment. \*Advances in Geosciences\*, 40, 1–9. <https://doi.org/10.5194/adgeo-40-1-2014>](#)

659

660 [D'Alessandro, A., Scudero, S., and Vitale, G. \(2019\). A review of the capacitive MEMS for seismology.](#)  
661 [Sensors, 19\(14\), 3093. <https://doi.org/10.3390/s19143093>](#)

662

663 [El-Sheimy, N., Yoon, S., and Jiang, Z. \(2020\). Inertial sensors technologies and error modelling for navigation](#)  
664 [and uncertainty analysis. \*Journal of Applied Geodesy\*, 14\(2\), 115–134. \[https://doi.org/10.1186/s43020-019-\]\(https://doi.org/10.1186/s43020-019-0001-5\)](#)  
665 [0001-5.](#)

666

667 [Kranzhoff, S. L., Lehmann, J., Kirchhoff, R., et al. \(2023\). A vertical inertial sensor with interferometric](#)  
668 [readout. \*Classical and Quantum Gravity\*, 40\(1\), 015007. <https://doi.org/10.1088/1361-6382/aca45b>](#)

669

670 [Maculotti, G., Elster, C., Wübbeler, G., et al. \(2024\). A shared metrological framework for trustworthy virtual](#)  
671 [experiments and digital twins. \*Metrology\*, 4\(3\), 337–363. <https://doi.org/10.3390/metrology4030021>.](#)

672

673 [Mitchell, A., et al. \(2025\). Integration of high-performance compact interferometric sensors in a suspended](#)  
674 [interferometer. \*Classical and Quantum Gravity\*, 42\(19\), 195014. <https://doi.org/10.1088/1361-6382/ac0087>](#)

675

676 [Oppenheim, A. V., & Schaffer, R. W. \(2010\). \*Discrete-Time Signal Processing\* \(3rd ed.\)](#)  
677 [Prentice Hall. ISBN: 9780131988424](#)

678

679 [Poroskun, I., Rothleitner, C., and Heißelmann, D. \(2022\). Structure of digital metrological twins as software](#)  
680 [for uncertainty estimation. \*Journal of Sensors and Sensor Systems\*, 11, 75–82. \[https://doi.org/10.5194/jsss-11-\]\(https://doi.org/10.5194/jsss-11-75-2022\)](#)  
681 [75-2022.](#)

682

ha formattato: Colore carattere: Testo 1

ha formattato: Colore carattere: Testo 1

ha formattato: Colore carattere: Testo 1

ha formattato: Colore carattere: Testo 1, Inglese (Stati Uniti)

ha formattato: Colore carattere: Testo 1

ha formattato: Colore carattere: Testo 1

ha formattato: Colore carattere: Testo 1

ha formattato: Colore carattere: Testo 1, Tedesco (Germania)

ha formattato: Colore carattere: Testo 1

ha formattato: Colore carattere: Testo 1

ha formattato: Colore carattere: Testo 1

683 Prasad, A., Middlemiss, R. P., Noack, A., *et al.* (2022). A 19 day earth tide measurement with a MEMS  
684 gravimeter. *Scientific Reports*, 12, 13091. <https://doi.org/10.1038/s41598-022-16881-1>

685

686 Ríos, J., Staudter, G., Weber, M., and Anderl, R. (2020). Uncertainty of data and the digital twin: a review.  
687 *International Journal of Product Lifecycle Management*, 12(4), 329–358.  
688 <https://doi.org/10.1504/IJPLM.2020.10035102>

689

690 Samadi, H., Ahsan, M. M., & Raman, S. (2025). Metrology and manufacturing-integrated digital twin (MM-  
691 DT) for advanced manufacturing: Insights from coordinate measuring machine (CMM) and FARO arm  
692 measurements. *Next Research*, 2(2), 100299. <https://doi.org/10.1016/j.nexres.2025.100299>

693

694 Sepahi-Boroujeni, S., & Khameneifar, F. (2024). Digital twin-enabled error and uncertainty mapping for 3D  
695 scanning. *Precision Engineering*. <https://doi.org/10.1016/j.precisioneng.2024.03.007>

696

697 Scholz, G., Fortmeier, I., Marschall, M., *et al.* (2022). Experimental design for virtual experiments in tilted-  
698 wave interferometry. *Metrology*, 2(1), 84–97. <https://doi.org/10.3390/metrology2010006>

699

700 Sider, A., Di Fronzo, C., Amez-Droz, L., *et al.* (2023). E-TEST: a compact low-frequency isolator for a large  
701 cryogenic mirror. *Classical and Quantum Gravity*, 40(16), 165002. <https://doi.org/10.1088/1361-6382/ace230>

702

703 Sun, Z., Wang, Q., Pan, J., *et al.* (2024). Review on digital twin applications and development challenges in  
704 structural monitoring. *Sensors*, 25(1), 59. <https://doi.org/10.3390/s25010059>

705

706 Ubezio, B., Ergun, S., and Zangl, H. (2023). Realistic sensor simulations for the digital twin.  
707 *e+i Elektrotechnik und Informationstechnik*, 140(10), 562–571. <https://doi.org/10.1007/s00502-023-01156-y>

708

709 Ubhi, A. S., Prokhorov, L., Cooper, S., *et al.* (2022). Active platform stabilization with a 6D seismometer.  
710 *Applied Physics Letters*, 121, 174101. <https://doi.org/10.1063/5.0118606>

ha formattato: Colore carattere: Testo 1, Inglese (Stati Uniti)

ha formattato: Colore carattere: Testo 1

ha formattato: Colore carattere: Testo 1, Inglese (Stati Uniti)

ha formattato: Colore carattere: Testo 1, Inglese (Stati Uniti)

ha formattato: Colore carattere: Testo 1

ha formattato: Colore carattere: Testo 1

ha formattato: Colore carattere: Testo 1

ha formattato: Colore carattere: Testo 1

ha formattato: Colore carattere: Testo 1

ha formattato: Colore carattere: Testo 1

ha formattato: Colore carattere: Testo 1

ha formattato: Colore carattere: Testo 1

ha formattato: Colore carattere: Testo 1

711

712 [van Dongen, J., et al. \(2023\). Reducing control noise in gravitational wave detectors with interferometric local](#)

713 [damping of suspended optics. \*Review of Scientific Instruments\*, 94\(5\), 054501.](#)

714 <https://doi.org/10.1063/5.0144865>

715

716 [Vlaeyen, M., et al. \(2021\). Digital twin of an optical measurement system.](#)

717 [Sensors, 21\(19\), 6638. <https://doi.org/10.3390/s21196638>](#)

718

719 [Wright, L., and Davidson, S. \(2024\). Digital twins for metrology; metrology for digital twins.](#)

720 [Measurement Science and Technology, 35. <https://doi.org/10.1088/1361-6501/ad2050>](#)

721

722 [Wübbeler, G., Marschall, M., Kniel, K., Heißelmann, D., Härtig, F., and Elster, C. \(2022\). GUM-Compliant](#)

723 [Uncertainty Evaluation Using Virtual Experiments. \*Metrology\*, 2\(1\), 114–127.](#)

724 <https://doi.org/10.3390/metrology201000>

725

726 [Zhao, G., et al. \(2022\). An interferometric inertial sensor for low-frequency seismic isolation.](#)

727 [Sensors and Actuators A: Physical, 335, 113398. <https://doi.org/10.1016/j.sna.2022.113398>](#)

728

729 [Yang, Z., Zhang, H., Xu, P., and Luo, Z. \(2023\). Unsupervised Noise Reductions for Gravitational Reference](#)

730 [Sensors or Accelerometers Based on the Noise2Noise Method. \*Sensors\*, 23\(13\), 6030.](#)

731 <https://doi.org/10.3390/s23136030>

**ha formattato:** Colore carattere: Testo 1, Francese (Francia)

**ha formattato:** Colore carattere: Testo 1, Inglese (Stati Uniti)

**ha formattato:** Colore carattere: Testo 1

**ha formattato:** Colore carattere: Testo 1

**ha formattato:** Colore carattere: Testo 1

**ha formattato:** Colore carattere: Testo 1

**ha formattato:** Colore carattere: Testo 1

**ha formattato:** Colore carattere: Testo 1, Inglese (Stati Uniti)

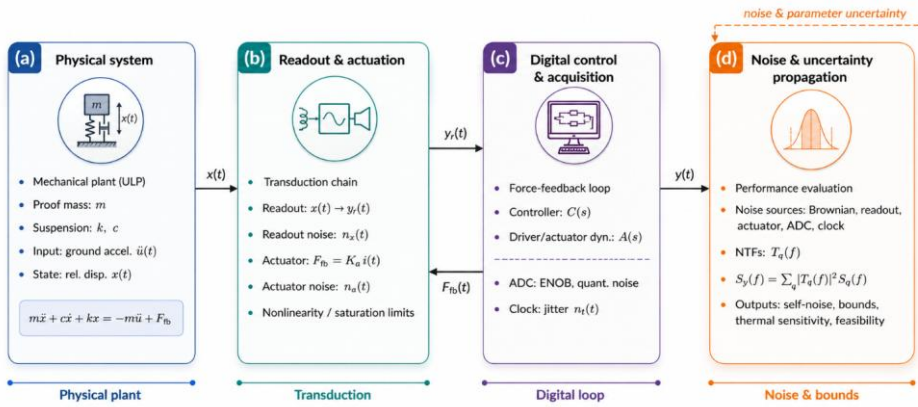
**ha formattato:** Colore carattere: Testo 1

**ha formattato:** Colore carattere: Testo 1

**ha formattato:** Colore carattere: Testo 1

**ha formattato:** Colore carattere: Testo 1, Inglese (Stati Uniti)

**ha formattato:** Colore carattere: Testo 1



732 **Figure 1.** Conceptual block diagram of the digital-twin framework adopted for the analysis and design of a  
 733 force-feedback ultra-long-period (ULP) seismometer. (a) Physical system: mechanical plant modeled as a  
 734 proof mass–spring–damper system, driven by ground acceleration and controlled via feedback force, described  
 735 by the equation of motion  $m\ddot{x} + c\dot{x} + kx = -m\ddot{u} + F_{fb}$ . (b) Readout and actuation: transduction chain  
 736 mapping the relative displacement  $x(t)$  into the readout signal  $y_r(t)$ , including readout noise and actuator  
 737 dynamics, force generation, and nonlinearity or saturation effects. (c) Digital control and acquisition: closed-  
 738 loop force-feedback architecture comprising the digital controller  $C(s)$ , driver/actuator dynamics  $A(s)$ ,  
 739 analog-to-digital conversion (ENOB and quantization noise), and clock jitter, yielding the output signal  $y(t)$  in  
 740 physical units. (d) Noise and uncertainty propagation: evaluation of the contribution of independent noise  
 741 sources (Brownian, readout, actuator, ADC, and clock) through their corresponding noise transfer functions  
 742  $T_q(f)$ , resulting in the output power spectral density  $S_y(f) = \sum_q |T_q(f)|^2 S_q(f)$ . The framework enables  
 743 quantitative assessment of self-noise, theoretical performance bounds, thermal sensitivity, and overall  
 744 feasibility of the instrument design.  
 745

ha formattato: Colore carattere: Testo 1

ha formattato: Colore carattere: Testo 1

ha formattato: Colore carattere: Testo 1

ha formattato: Colore carattere: Testo 1

ha formattato: Colore carattere: Testo 1

ha formattato: Colore carattere: Testo 1

ha formattato: Colore carattere: Testo 1

ha formattato: Colore carattere: Testo 1

ha formattato: Colore carattere: Testo 1

ha formattato: Colore carattere: Testo 1

ha formattato: Colore carattere: Testo 1

ha formattato: Colore carattere: Testo 1

ha formattato: Colore carattere: Testo 1

ha formattato: Colore carattere: Testo 1

ha formattato: Colore carattere: Testo 1

ha formattato: Colore carattere: Testo 1

ha formattato: Colore carattere: Testo 1

ha formattato: Colore carattere: Testo 1

ha formattato: Colore carattere: Testo 1

ha formattato: Colore carattere: Testo 1

ha formattato: Colore carattere: Testo 1

ha formattato: Colore carattere: Testo 1

ha formattato: Colore carattere: Testo 1

ha formattato: Colore carattere: Testo 1

ha formattato: Colore carattere: Testo 1

ha formattato: Colore carattere: Testo 1

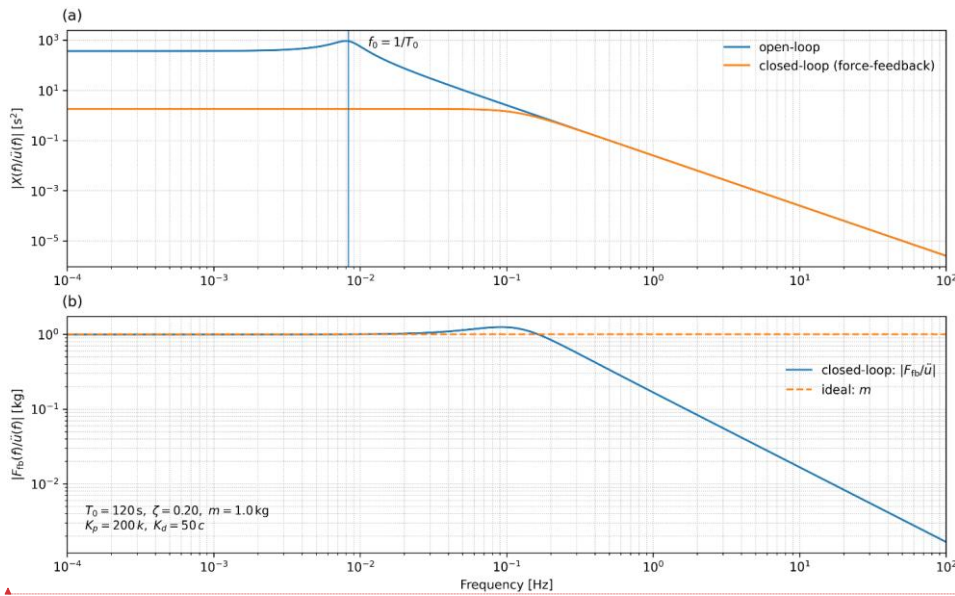
ha formattato: Colore carattere: Testo 1

ha formattato: Colore carattere: Testo 1

ha formattato: Colore carattere: Testo 1

ha formattato: Colore carattere: Testo 1

ha formattato: Colore carattere: Testo 1



746 **Figure 2.** Frequency-domain response of the ultra-long-period (ULP) force-feedback seismometer digital twin.  
 747 (a) Magnitude of the mechanical compliance  $|X(f)/\ddot{u}(f)|$ , comparing the open-loop response of the  
 748 mechanical plant with the closed-loop response obtained through force-feedback control. The open-loop  
 749 resonance at the natural frequency  $f_0 = 1/T_0$  is clearly visible, while the closed-loop configuration suppresses  
 750 the resonance and significantly reduces proof-mass motion over a broad frequency band. (b) Magnitude of the  
 751 force-balance transfer function  $|F_{fb}(f)/\ddot{u}(f)|$  in the closed-loop configuration, compared with the ideal low-  
 752 frequency limit  $F_{fb}/\ddot{u} = m$ . At low frequencies, the feedback force accurately tracks the inertial force  
 753 associated with ground acceleration, whereas at higher frequencies the response rolls off due to the finite  
 754 bandwidth of the control loop. The parameters reported in the inset correspond to a representative ULP  
 755 configuration and a proportional-derivative feedback law.  
 756

ha formattato: Colore carattere: Testo 1

ha formattato: Colore carattere: Testo 1

ha formattato: Colore carattere: Testo 1

ha formattato: Colore carattere: Testo 1

ha formattato: Colore carattere: Testo 1

ha formattato: Colore carattere: Testo 1

ha formattato: Colore carattere: Testo 1

ha formattato: Colore carattere: Testo 1

ha formattato: Colore carattere: Testo 1

ha formattato: Colore carattere: Testo 1

ha formattato: Colore carattere: Testo 1

ha formattato: Colore carattere: Testo 1

ha formattato: Colore carattere: Testo 1

ha formattato: Colore carattere: Testo 1

ha formattato: Colore carattere: Testo 1

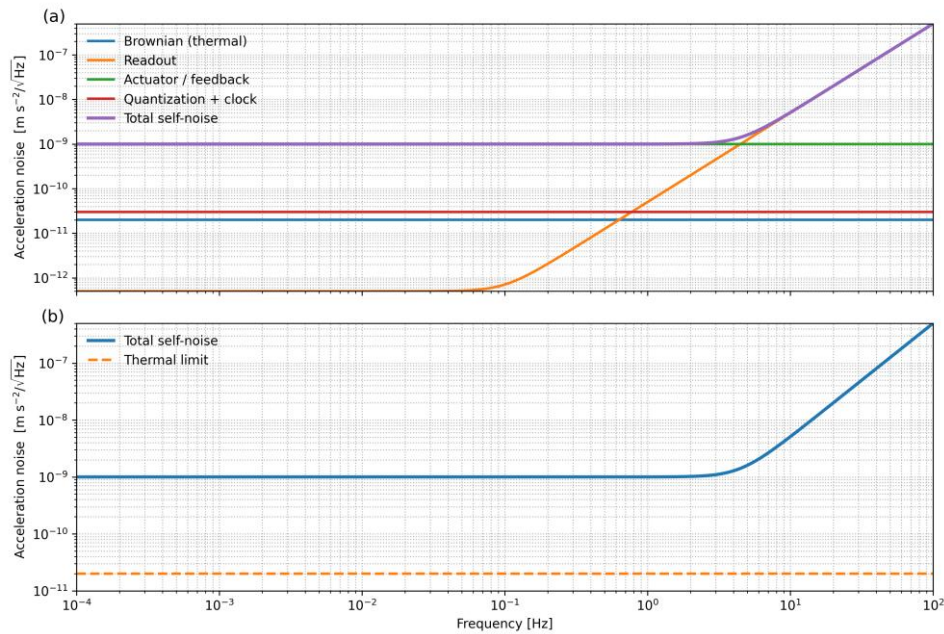
ha formattato: Colore carattere: Testo 1

ha formattato: Colore carattere: Testo 1

ha formattato: Colore carattere: Testo 1

ha formattato: Colore carattere: Testo 1

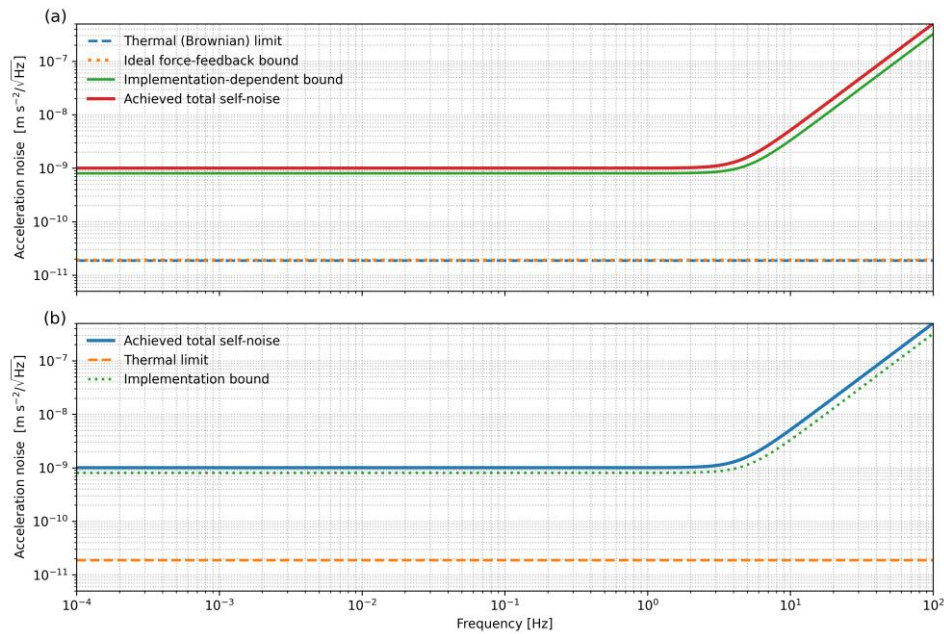
ha formattato: Colore carattere: Testo 1



757  
 758 **Figure 3.** Frequency-dependent acceleration self-noise budget of the force-feedback ULP seismometer derived  
 759 from the digital-twin framework. (a) Individual noise contributions referred to input acceleration, including  
 760 Brownian (thermal) noise of the mechanical plant, readout noise, actuator/feedback noise, and quantization  
 761 plus clock jitter, together with their quadratic sum defining the total self-noise. The spectrum highlights the  
 762 transition from readout- and quantization-limited performance at low frequencies to feedback- and control-  
 763 limited behavior at higher frequencies. (b) Comparison between the total self-noise and the fundamental  
 764 thermal limit set by the mechanical suspension. Model parameters are indicated in the panel and correspond  
 765 to a nominal ultra-long-period design with force-feedback control. The separation between the total self-noise  
 766 and the thermal limit quantifies the residual performance gap attributable to non-thermal noise sources and  
 767 control-loop implementation.

ha formattato: Colore carattere: Testo 1

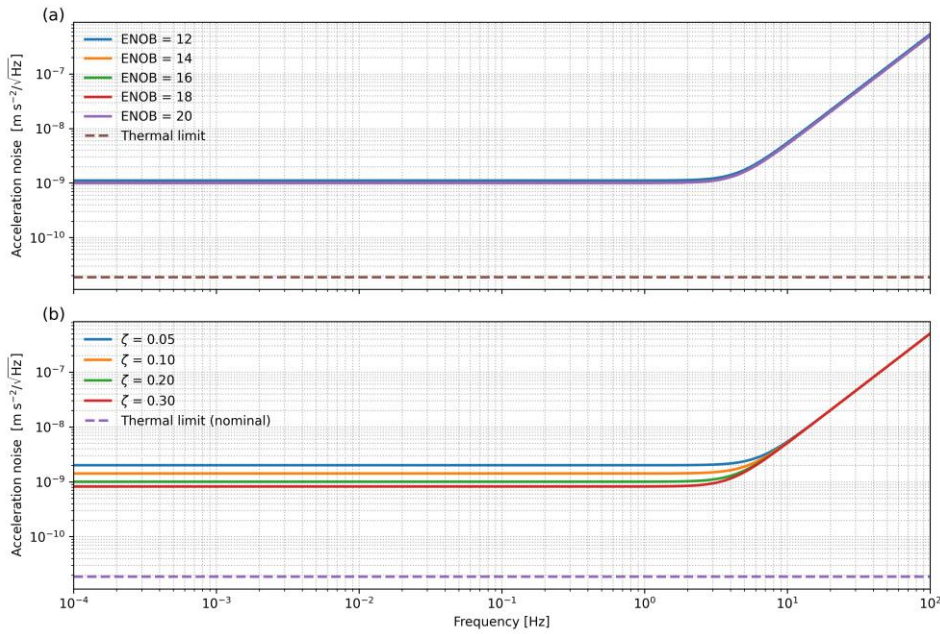
ha formattato: Colore carattere: Testo 1



768 **Figure 4.** Metrological acceleration-noise bounds and achieved performance of the force-feedback ultra-long-  
 769 period (ULP) seismometer derived from the digital-twin framework. (a) Fundamental and implementation-  
 770 dependent noise bounds referred to input acceleration. The thermal (Brownian) limit represents the irreducible  
 771 noise floor imposed by mechanical dissipation in the suspension. The ideal force-feedback bound coincides  
 772 with the thermal limit in the absence of electronic and control noise and is shown with a slight offset for visual  
 773 clarity. The implementation-dependent bound accounts for practical non-idealities introduced by actuation,  
 774 digitization, timing, and control-loop dynamics, and exhibits a frequency-dependent rise imposed by closed-  
 775 loop causality. The achieved total self-noise is shown for reference. (b) Comparison between the achieved total  
 776 self-noise and the theoretical bounds. The separation from the thermal limit quantifies the residual  
 777 performance gap attributable to control-loop implementation and electronic noise sources, providing a direct  
 778 metric to assess design margins and guide further optimization toward fundamental physical limits.  
 779

ha formattato: Colore carattere: Testo 1

ha formattato: Colore carattere: Testo 1



780  
 781 **Figure 5.** Spectral sensitivity of the closed-loop instrument self-noise to key design parameters. (a) Total  
 782 acceleration self-noise amplitude spectral density  $S_{\ddot{a}}^{\text{self}}(\omega)N_{\text{a}}(\omega)$  for different effective ADC resolutions (ENOB  
 783 = 12–20 bits), computed for a fixed mechanical plant ( $m = 1 \text{ kg}$ ,  $T_{\text{0}} = 120 \text{ s}$ ,  $\zeta = 0.20$ ) and identical control  
 784 architecture. At low frequencies the spectra collapse onto a common plateau set by non-digital noise sources,  
 785 whereas at higher frequencies the achievable noise floor progressively improves with increasing ENOB as  
 786 quantization and digital-chain contributions are reduced. The dashed curve indicates the Brownian (thermal)  
 787 acceleration limit, shown for reference. (b) Sensitivity of the total acceleration self-noise to the damping ratio  
 788  $\zeta$  (0.05–0.30) at fixed ENOB (16 bits). Variations in  $\zeta$  primarily affect the low-frequency noise level through the  
 789 balance between thermal dissipation and feedback-related contributions, while the high-frequency rise  
 790 remains controlled by the digital and readout bandwidth. The dashed line marks the nominal thermal limit.  
 791 Together, the two panels illustrate how electronic resolution and mechanical damping act on distinct frequency  
 792 regimes, defining complementary design trade-offs for ultra-low-frequency force-feedback inertial sensors.

ha formattato: Colore carattere: Testo 1

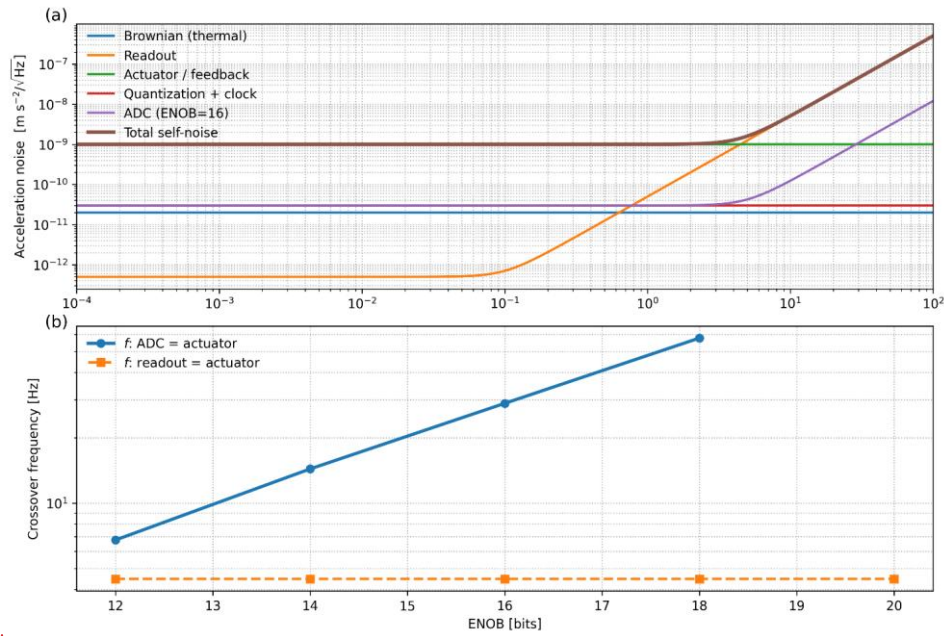
ha formattato: Colore carattere: Testo 1

ha formattato: Colore carattere: Testo 1

ha formattato: Colore carattere: Testo 1

ha formattato: Colore carattere: Testo 1

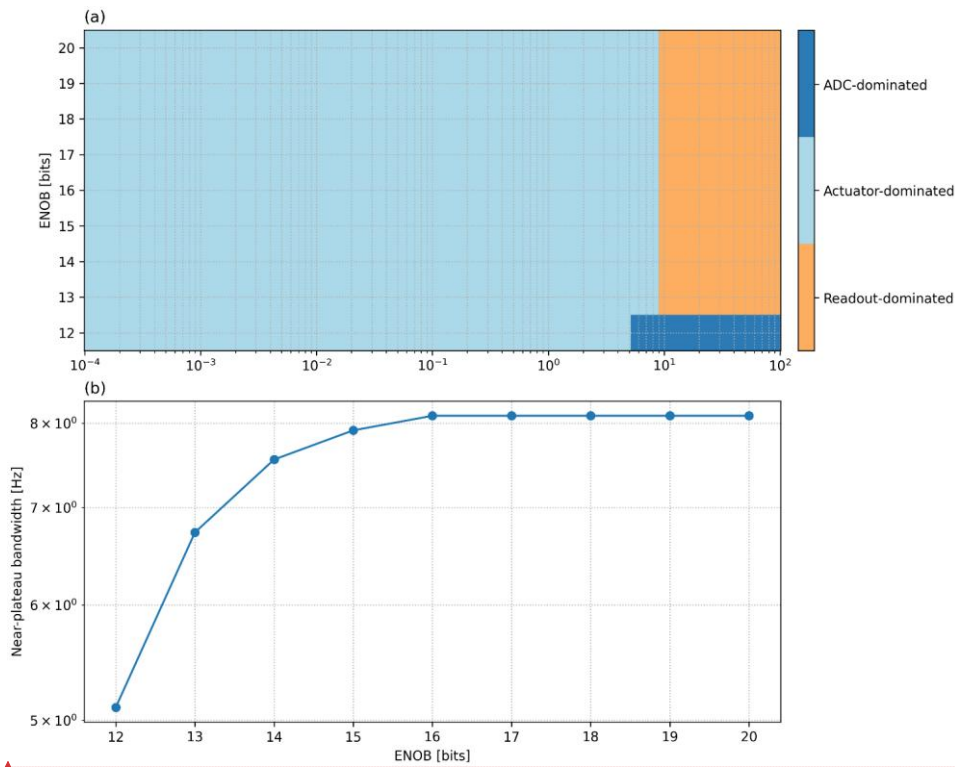
ha formattato: Colore carattere: Testo 1



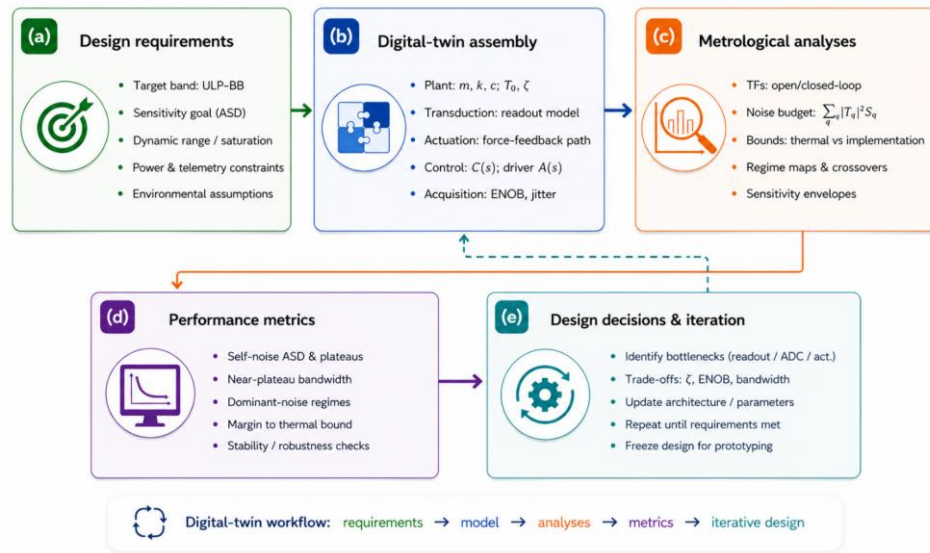
793 **Figure 6.** Noise regimes and crossover frequencies in a digitally controlled broadband inertial sensor. (a)  
 794 Acceleration noise amplitude spectral density (ASD) as a function of frequency, showing the individual  
 795 contributions from Brownian (thermal) noise, readout noise, actuator/feedback noise, quantization and clock  
 796 noise, and the digital (ADC) contribution for a nominal resolution of ENOB = 16 bits. The resulting total self-  
 797 noise (quadratic sum of all components) is also shown. The plot highlights the frequency-dependent dominance  
 798 of different noise sources, with readout noise governing the low-frequency range, actuator/feedback noise  
 799 setting the mid-band floor, and digital/ADC-related effects becoming relevant at higher frequencies due to  
 800 closed-loop shaping. (b) Crossover frequencies between selected noise contributions as a function of effective  
 801 ADC resolution (ENOB). The blue curve indicates the frequency at which ADC noise equals actuator/feedback  
 802 noise, demonstrating the systematic extension of the near-thermal bandwidth with increasing ENOB. The  
 803 orange curve shows the crossover between readout and actuator noise, which remains nearly invariant with  
 804 ENOB, reflecting its weak dependence on digitization resolution. Together, panels (a) and (b) illustrate how  
 805 digital resolution primarily controls the high-frequency noise budget, while low- and mid-band performance  
 806 are constrained by analog sensing and actuation mechanisms.  
 807

ha formattato: Colore carattere: Testo 1

ha formattato: Colore carattere: Testo 1



808  
 809 **Figure 7.** Design regime map and effective near-plateau bandwidth. (a) Dominant self-noise contributor in  
 810 the ENOB–frequency plane, classified by variance comparison between readout, actuator/feedback, and ADC  
 811 noise terms. The map highlights distinct operating regimes and shows that, for typical design parameters, the  
 812 system is predominantly actuator-limited over most of the seismic bandwidth, with ADC-dominated behavior  
 813 confined to low ENOB and high frequencies, and readout domination emerging at the highest frequencies. (b)  
 814 Near-plateau bandwidth as a function of ENOB, defined as the frequency range over which the total self-noise  
 815 remains within 30% of its minimum achievable plateau. Increasing ENOB significantly extends the usable low-  
 816 noise bandwidth up to  $ENOB \approx 15\text{--}16$ , beyond which further improvements yield diminishing returns,  
 817 indicating a transition to actuator/readout-limited performance. This representation provides a compact and  
 818 quantitative guideline for digitization requirements in force-feedback broadband sensors.



ha formattato: Colore carattere: Testo 1

ha formattato: Colore carattere: Testo 1

























819


820 **Figure 8.** Conceptual workflow of the digital-twin framework adopted for the engineering design and  
 821 metrological assessment of ultra-low-noise broadband inertial sensors. (a) Definition of design requirements,  
 822 including target bandwidth, sensitivity objectives, dynamic range constraints, and environmental assumptions.  
 823 (b) Assembly of the digital twin, integrating the mechanical plant, transduction chain, force-feedback  
 824 actuation, control architecture, and acquisition system. (c) Metrological analyses performed in the frequency  
 825 domain, encompassing open- and closed-loop transfer functions, full noise-budget decomposition, and  
 826 theoretical versus implementation-dependent performance bounds. (d) Extraction of performance metrics,  
 827 such as self-noise plateaus, near-plateau bandwidth, dominant noise regimes, and margins relative to the  
 828 thermal limit. (e) Iterative design loop, where identified bottlenecks guide trade-offs among damping, ENOB,  
 829 and bandwidth, leading to progressive architectural refinement and final design freeze. Solid arrows indicate  
 830 the nominal forward workflow, whereas the dashed arrow highlights the feedback loop driving iterative  
 831 optimization.

832

ha formattato: Colore carattere: Testo 1

ha formattato: Colore carattere: Testo 1

	<b>Traditional Noise Budgeting</b> <i>Component-wise approach</i>	<b>Simplified Digital Twin Models</b> <i>Subsystem-based or non-causal</i>	<b>Proposed Framework</b> <i>Causal and Uncertainty-Aware Digital Twin</i>
 <b>Physical causality</b>	 <b>Not explicitly enforced</b> Assumes ideal transformations and post-processing inversions.	 <b>Partially enforced or neglected</b> Often relies on idealized or non-causal inversions.	 <b>Explicitly enforced</b> All transformations are causal and physically realizable.
 <b>System-level coupling</b>	 <b>Neglected or approximated</b> Interactions between mechanical, electrical, and digital domains are not fully captured.	 <b>Subsystem-based</b> Models individual blocks; weak representation of cross-domain coupling and feedback.	 <b>Fully integrated</b> Mechanical, electrical, and digital domains are coupled through closed-loop dynamics.
 <b>Uncertainty propagation</b>	 <b>Limited</b> Uncertainties treated independently for each component; correlations typically ignored.	 <b>Limited or qualitative</b> Uncertainty usually assessed qualitatively or with simplified assumptions.	 <b>Systematic and distribution-based</b> Uncertainty propagated through all transfer functions using Monte Carlo analysis.
 <b>Noise modeling consistency</b>	 <b>Additive and a posteriori</b> Noise contributions added after independent evaluation of subsystems.	 <b>May include idealizations</b> Noise modeled with simplifications; non-causal operations may be introduced.	 <b>Fully consistent</b> All noise sources mapped through their physical transfer functions in a unified framework.
 <b>Performance metrics</b>	 <b>Component-level only</b> Provides individual noise floors but no system-level metrics such as crossover frequencies.	 <b>Limited system-level metrics</b> Provides global sensitivity estimates but typically lacks bandwidth-related metrics.	 <b>Advanced system-level metrics</b> <ul style="list-style-type: none"><li>• Crossover frequencies (Eq. 7)</li><li>• Near-plateau bandwidth (Eq. 8)</li><li>• Thermal ratio metrics (Eq. 6, 10)</li></ul>
 <b>Typical limitations</b>	 <b>Ignores feedback coupling and closed-loop effects</b> May lead to inconsistent or non-realizable performance predictions.	 <b>Can lead to optimistic performance predictions</b> Non-causal modeling may violate realizability and physical constraints.	 <b>Increased model complexity</b> Requires accurate parameterization and computational resources.

**Increasing physical consistency and predictive capability** 

833

834

835

836

837

838

839

840

841

842

**Figure 9.** Comparative assessment of sensor design methodologies for ultra-low-noise inertial systems. The diagram contrasts traditional noise budgeting, simplified digital twin approaches, and the proposed causal and uncertainty-aware digital-twin framework in terms of physical causality, system-level coupling, uncertainty propagation, noise modeling consistency, and performance metrics. Conventional approaches either neglect feedback-induced coupling or rely on simplified or non-causal representations, limiting their ability to provide consistent system-level predictions. In contrast, the proposed framework enforces causal dynamics and propagates all noise sources through a unified transfer-function representation, enabling physically consistent evaluation and the definition of advanced performance metrics such as crossover frequencies and near-plateau bandwidth.